

SCIENTIFIC REPORTS

OPEN

Characterization and Modeling of Nonfilamentary Ta/TaO_x/TiO₂/Ti Analog Synaptic Device

Yu-Fen Wang, Yen-Chuan Lin, I-Ting Wang, Tzu-Ping Lin & Tuo-Hung Hou

Received: 08 January 2015

Accepted: 31 March 2015

Published: 08 May 2015

A two-terminal analog synaptic device that precisely emulates biological synaptic features is expected to be a critical component for future hardware-based neuromorphic computing. Typical synaptic devices based on filamentary resistive switching face severe limitations on the implementation of concurrent inhibitory and excitatory synapses with low conductance and state fluctuation. For overcoming these limitations, we propose a Ta/TaO_x/TiO₂/Ti device with superior analog synaptic features. A physical simulation based on the homogeneous (nonfilamentary) barrier modulation induced by oxygen ion migration accurately reproduces various DC and AC evolutions of synaptic states, including the spike-timing-dependent plasticity and paired-pulse facilitation. Furthermore, a physics-based compact model for facilitating circuit-level design is proposed on the basis of the general definition of memristor devices. This comprehensive experimental and theoretical study of the promising electronic synapse can facilitate realizing large-scale neuromorphic systems.

Energy-efficient, fault-tolerant, massively parallel neuromorphic computing [1] is a computing paradigm that is superior to conventional computers in adaptively processing unstructured and imprecise sensory inputs and performing tasks, such as pattern and voice recognition, robot control, and navigation. Among various implementation technologies, synaptic electronics is an emerging technology aimed at facilitating neuromorphic computing through the use of bio-inspired hardware systems [2]. The main device component in synaptic electronics is a low-power, analog electronic synapse, the so-called memristor [3,4], which emulates both the functionality and the two-terminal structure of a biological synapse. A resistive random access memory (RRAM)-based synapse [5–14] exhibits excellent scaling potential beyond 10 nm [15], a compact 4F² cell size, full CMOS compatibility, ultralow energy consumption per synaptic operation on the order of picojoules [8], and capability of realizing three-dimensional (3D) neural network [9]. These features outperform those of other electronic synapse candidates based on phase-change memory [16,17], ferroelectric memory [18], and floating-gate devices [19]. Most RRAM-based synaptic devices utilize the filamentary conduction mechanism [20], which leads to the following limitations: (1) Many filamentary synaptic devices exhibit gradual RESET but abrupt SET characteristics [5–9]. Implementing concurrent inhibitory and excitatory synapses is not possible, which may hinder the full potential of neuromorphic computing. (2) Because of the filamentary conduction, reducing the synaptic conductance in aggressively scaled devices is difficult. High conductance poses challenges in reducing power consumption, and device characteristics are more susceptible to parasitic line resistance in high-density neural networks. Furthermore, the area overhead of leaky integrate-and-fire neuron circuits becomes appreciable because a larger capacitor is required to integrate the high current. (3) The multiple conductance states of filamentary synaptic devices are controlled by an extremely low number of defects in the nanoscale filament [21]. Therefore, these devices are subjected to large conductance fluctuations because of the intrinsic randomness of defect numbers, especially in the low conductance regime [8–11]. Although the neuromorphic system is fault-tolerant, a high degree of conductance fluctuations still adversely affects

Department of Electronics Engineering and Institute of Electronics, National Chiao Tung University, Hsinchu, Taiwan. Correspondence and requests for materials should be addressed to T.H.H. (email: thhou@mail.nctu.edu.tw)

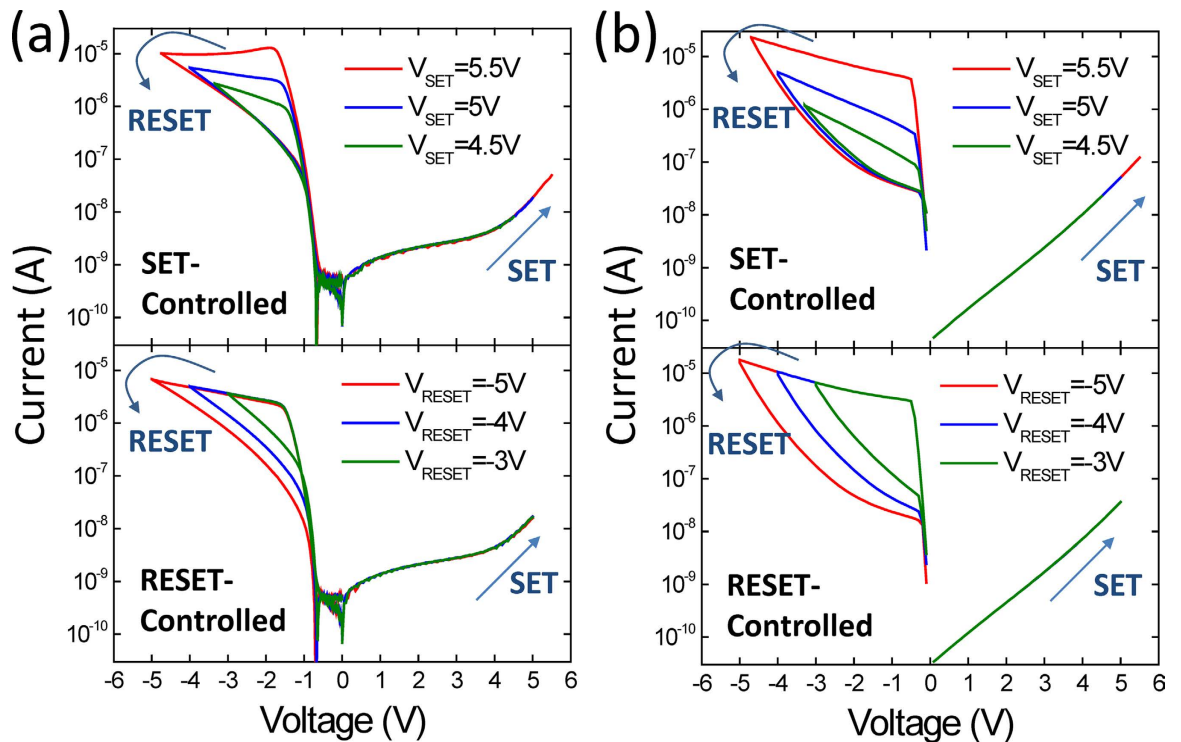


Figure 1. Multiple resistance states by DC voltage sweep and simulation results. (a) Typical bipolar resistive-switching I - V curves of the Ta/TaO_x/TiO₂/Ti device. Multiple resistance states were controlled by employing a gradual SET process in which various SET voltages were used (SET-controlled mode) and a gradual RESET process in which various RESET voltages were used (RESET-controlled mode). The conditions for the SET-controlled mode were $V_{\text{SET}}=5.5\text{ V}$, $V_{\text{RESET}}=-4.75\text{ V}$; $V_{\text{SET}}=5\text{ V}$, $V_{\text{RESET}}=-4\text{ V}$; $V_{\text{SET}}=4.5\text{ V}$, $V_{\text{RESET}}=-3.35\text{ V}$. The conditions for the RESET-controlled mode were $V_{\text{SET}}=5\text{ V}$, $V_{\text{RESET}}=-5\text{ V}$; $V_{\text{SET}}=5\text{ V}$, $V_{\text{RESET}}=-4\text{ V}$; $V_{\text{SET}}=5\text{ V}$, $V_{\text{RESET}}=-3\text{ V}$. (b) Simulation of SET-controlled and RESET-controlled multiple resistance states using the HBM model. The main device features were successfully reproduced.

computational accuracy [9]. For overcoming these limitations, new studies have explored RRAM-based synaptic devices that utilize nonfilamentary (homogeneous) switching mechanisms [12–14]. However, exotic materials, such as praseodymium calcium manganese oxide (PCMO) [12,13], and processes incompatible with semiconductor fabrication, such as sol-gel [14], are often required for fabricating these devices, thus posing additional challenges for high-density integration. Furthermore, the device characteristics and operating mechanism of such nonfilamentary RRAM-based synaptic devices are considerably less understood compared with those of filamentary RRAM-based synaptic devices.

Recently, a Ta/TaO_x/TiO₂/Ti device has shown great potential for implementing high-density crossbar memory arrays with numerous highly desirable features including extremely high endurance, forming-free, self-compliance, self-rectification, multiple-level-per-cell capability, and a semiconductor-friendly material and fabrication process [22,23]. The resistance change in this device is determined by homogeneous barrier modulation (HBM) induced by oxygen ion migration [23]. In this paper, we report an experimental and theoretical study of analog synaptic features in the Ta/TaO_x/TiO₂/Ti device. Because of its nonfilamentary mechanism, this device overcomes the limitations of conventional filamentary synaptic devices and shows promising properties for neuromorphic computing, including concurrent inhibitory and excitatory synaptic plasticity, and low synaptic conductance with minimal fluctuation. We present a physical model of HBM that quantitatively describes both the steady-state (DC) and dynamic (AC) evolution of synaptic states. Furthermore, we propose an analytical compact model based on the physical model of HBM and the general definition of memristor devices to facilitate circuit-level simulations in future large-scale neuromorphic system designs.

Results

The studied Ta/TaO_x/TiO₂/Ti device (see Methods Section) exhibits multiple resistance states that are adjustable by either the SET strength or RESET strength. Figure 1a shows typical current-voltage (I - V) curves of multiple resistance states, which can be precisely controlled by appropriate SET and RESET voltages. The operating conditions were chosen to show that an identical high-resistance-state (HRS) can be set to different low-resistance states (LRS's) by using different SET strengths and that, similarly, an

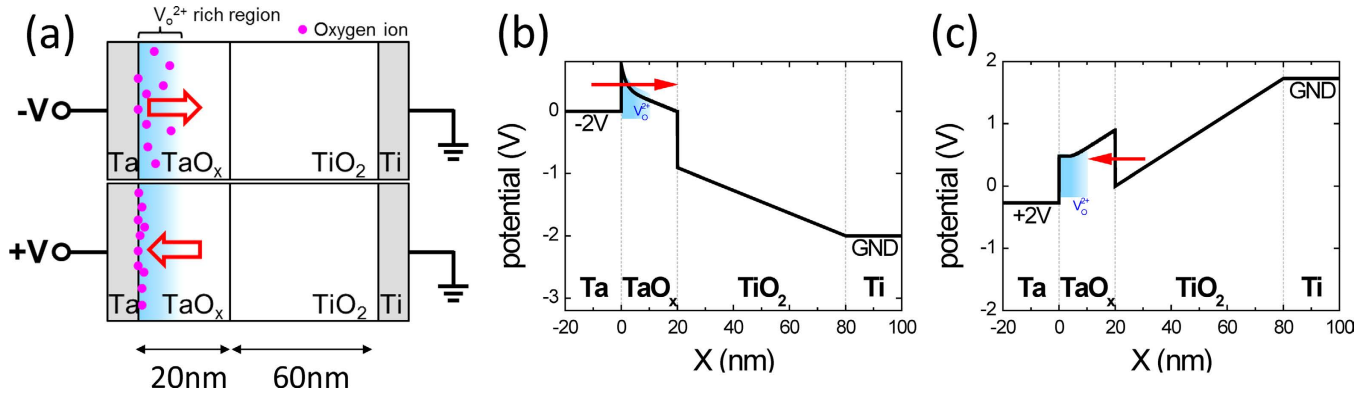


Figure 2. O^{2-} migration and homogeneous barrier modulation model. (a) Schematic diagrams showing O^{2-} migration in the V_O -rich (oxygen-deficient) layer near the Ta electrode during bipolar SET and RESET operations. Calculated band diagrams of low resistance state (after SET) at (b) -2V read and (c) $+2\text{V}$ read. At -2V read, the effective barrier width of electron tunneling from Ta was modulated by considering the charge distribution near the Ta/TaO_x interface. At $+2\text{V}$ read, the higher TaO_x/TiO₂ barrier suppressed electron tunneling into TaO_x, and the barrier modulation effect at the Ta/TaO_x interface had a negligible effect.

identical LRS can be reset to different HRS's by using different RESET strengths. Because of the rectifying I - V characteristics, the resistance states can be read out only at a negative voltage, and the SET transition is less apparent. An effective SET process requires at least $+4\text{V}$ (see Figure S1 in Supplementary Information). The HBM-based switching mechanism illustrated in Fig. 2 is supported by experimental current transport [23]. Because of the strong oxygen scavenging capability of Ta, an oxygen vacancy (V_O)-rich TaO_x region containing a substantial number of nonlattice oxygen ions (O^{2-}) exists near the Ta electrode (the blue region in Fig. 2a). For simplicity, negatively charged O^{2-} is assumed to migrate easily under local electric field F in V_O -rich TaO_x, and V_O are treated as immobile shallow donor-like dopants. During RESET at a negative voltage, O^{2-} migrates toward the bulk of the V_O -rich TaO_x region, thereby increasing the effective barrier width of electron tunneling from Ta into TaO_x and decreasing the device conductance at a negative read voltage. During SET at a positive voltage, O^{2-} migrates toward the interface of Ta and TaO_x, thereby decreasing the effective barrier width of electron tunneling and increasing the device conductance at a negative read voltage. Furthermore, the barrier modulation effect at the Ta/TaO_x interface has little influence on the electron tunnel barrier between TiO₂ and TaO_x, and a high TaO_x/TiO₂ barrier considerably suppresses the current at a positive read voltage, resulting in the characteristic rectifying I - V curve of the Ta/TaO_x/TiO₂/Ti device.

A one-dimensional (1D) simulation was performed to validate the proposed HBM model. O^{2-} migration was described using the diffusion and drift components of O^{2-} hopping through local potential wells [24,25]. The O^{2-} density (N_O) is obtained using the continuity equation as follows:

$$\frac{\partial N_\text{O}}{\partial t} = D \frac{\partial^2 N_\text{O}}{\partial x^2} - v \frac{\partial N_\text{O}}{\partial x} \quad (1)$$

The diffusion coefficient is obtained using $D = 1/2 a^2 f \cdot \exp(-E_a/kT)$, and the drift velocity is expressed as $v = a f \cdot \exp(-E_a/kT) \cdot \sinh(-q \gamma a F/kT)$, where a (0.05 nm) is the effective hopping distance and also the mesh size of numerical calculation [23,26], f (10^{13} Hz) is the attempt-to-escape frequency [23,26], kT ($T = 300\text{K}$) is the thermal energy, q is the elementary charge, γ is a fitting parameter used to account for the field dependence, and F is the electric field; E_a is the activation energy of migration, and it is assumed to be 0.65 eV [23] in the region where the V_O density (N_V) is greater than $2 \times 10^{20} \text{cm}^{-3}$, and to be 2 eV in the region where N_V is lower than $2 \times 10^{20} \text{cm}^{-3}$. It is well known that oxygen diffusion is much faster in nonstoichiometric metal oxides than that in stoichiometric oxides because of the high concentration of oxygen defects [27,28], and this fact is considered using this simplifying assumption on E_a . More discussions on the choice of simulation parameters can be found in Supplementary Information. N_V is assumed using an exponentially decaying function, with the highest N_V being at the Ta/TaO_x interface, which agrees with the gradient substoichiometric TaO_x composition observed experimentally [23]. The immobile shallow donor-like V_O is positively charged (V_O^{2+}) at nonzero F . The Poisson equation is solved for the entire Ta/TaO_x/TiO₂/Ti stack by considering the effect of both N_O and V_O^{2+} density (N_{V^+}) as:

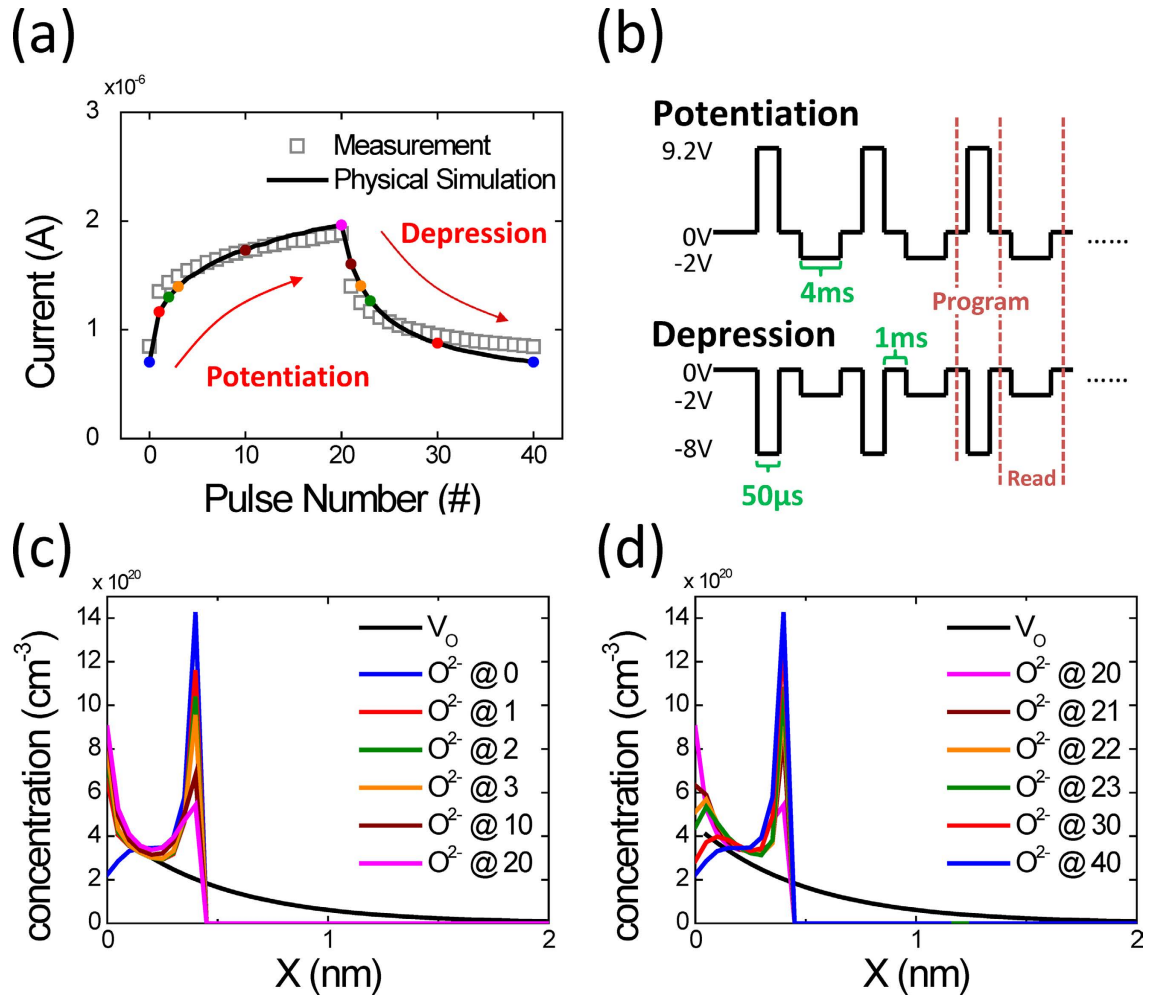


Figure 3. Potentiation and depression by applying AC pulse. (a) Measured and simulated potentiating (1st pulse to 20th pulse) and depressing (21st pulse to 40th pulse) curves of the Ta/TaO_x/TiO₂/Ti device, obtained by applying AC pulses successively. (b) The AC pulse waveforms used for potentiation and depression. A read pulse of -2V was applied to measure the cell conductance after every potentiating and depressing pulse. All time intervals between read or write pulses were 1 ms. The evolution of O²⁻ concentration near the Ta/TaO_x interface is shown for (c) the 1st potentiating pulse to the 20th potentiating pulse and (d) the 21st depressing pulse to the 40th depressing pulse. Charge accumulation at the Ta/TaO_x interface and at the low- E_a TaO_x/high- E_a TaO_x interface reduced the internal electric field and suppressed further O²⁻ migration, resulting in the conductance change saturating during potentiation and depression.

$$\frac{\partial F}{\partial x} = \frac{2q}{\epsilon_r \epsilon_0} (-N_O + N_{V+}) \quad (2)$$

where ϵ_r is the dielectric constant of TaO_x or TiO₂ and ϵ_0 is the permittivity of vacuum. After obtaining the potential profile across the device stack, the tunnel current through the TaO_x barrier is calculated using the Wentzel-Kramers-Brillouin (WKB) approximation and considering the field-dependent barrier lowering and the thermionic emission component. Figure 1b displays the DC I - V curves of SET-controlled and RESET-controlled multiple resistance states, obtained from the simulation; the curves show reasonable agreement with the experiments. The discrepancies in the calculated current in the high resistance state and the rectifying condition at a positive bias are attributed to defect-assisted transport processes other than tunneling in TaO_x.

The gradual transition among multiple resistance states induced by the SET and RESET strengths can be applied to implement concurrent inhibitory and excitatory synapses where the synaptic conductance can be increased and decreased using potentiating and depressing AC pulses, respectively. Increasing the number of pulses progressively is equivalent to programming the cell at a higher voltage because of the voltage and time dependence of ion migration [29]. Figure 3a,b show the measured potentiating and

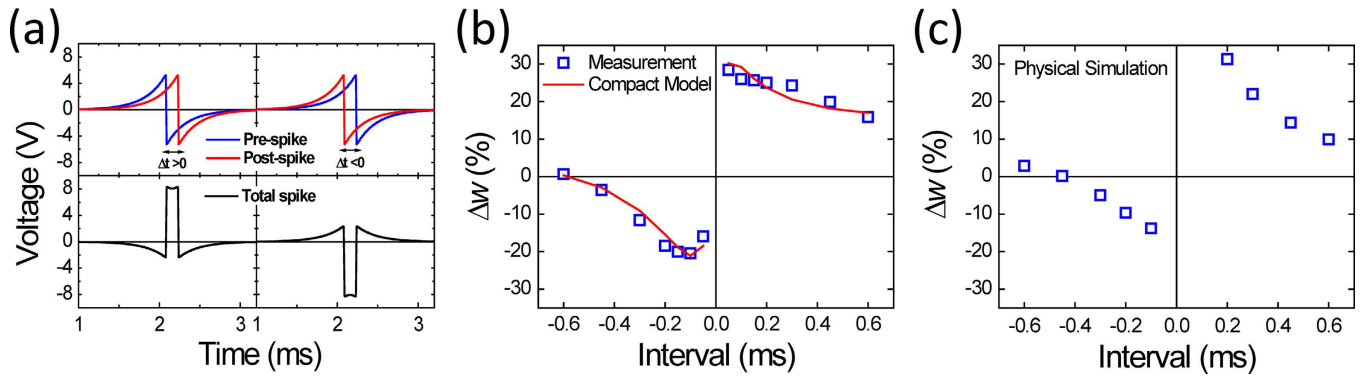


Figure 4. Spike-timing-dependent plasticity (STDP). (a) Biomorphic-action-potential-like waveforms used for STDP measurement and simulation. The pre-spike pulse was applied to the Ta electrode, and the post-spike pulse was applied to the Ti electrode. The potentiation and depression actions were controlled by the relative timing of the pre- and post-spikes (Δt). The synapse weight change (Δw) was positive for $\Delta t > 0$, whereas it was negative for $\Delta t < 0$. (b) The measured Δw as a function of Δt for the Ta/TaO_x/TiO₂/Ti device. The red line shows the fitting result of using the physics-based compact model. (c) Simulation results for STDP, obtained by considering oxygen ion migration and the homogeneous barrier modulation model.

depressing curves using consecutive AC pulses and the corresponding pulse waveforms. A read pulse of -2 V was applied to measure the cell conductance after every potentiating and depressing pulse. The 1D simulation result showed excellent agreement with the AC pulse measurement, validating the HBM model under both steady-state and transient conditions. The conductance change is not linearly proportional to the pulse number. The first few potentiating or depressing pulses exert considerably strong effects, and the change in the cell conductance gradually saturates. The nonlinearity in the potentiating and depressing curves is similar to those reported in other RRAM-based synapses [8–14], and it can be explained by the evolution of O²⁻ during potentiating and depression, as shown in Fig. 3c,d. O²⁻ migration occurs easily in the low- E_a region with a high V_O concentration. At the first potentiating pulse, O²⁻ moves rapidly from the TaO_x bulk toward the Ta/TaO_x interface. The conductance change saturates because charge accumulation reduces the internal electric field and suppresses further O²⁻ migration toward the interface. A similar phenomenon can also be cited to explain the saturation of the depression curve. Furthermore, in contrast to the large and random pulse-to-pulse conductance fluctuations in typical filamentary synapses [8–11], the conductance in the Ta/TaO_x/TiO₂/Ti device shows smooth and monotonic transitions between consecutive pulses, which is desirable for improving the learning accuracy in neuromorphic systems. The negligible pulse fluctuation is attributed to the higher number of ions involving in the state change.

The synaptic weight w in a biological neural network is modulated using the spike-timing-dependent plasticity (STDP), and it is typically measured according to the cell conductance. Instead of the square pulses shown in Fig. 3b, biological STDP is triggered by the relative timing of pre- and post-synaptic spikes [30]. STDP facilitates the Hebbian learning rule [31]; therefore, it is a critical function for learning and memory. The STDP characteristics of the Ta/TaO_x/TiO₂/Ti device were measured using a biomorphic-action-potential-like waveform (Fig. 4a), which was generated using:

$$V = \begin{cases} A \cdot \exp(-t/\tau), & t > 0 \\ -A \cdot \exp(-t/\tau), & t < 0 \end{cases} \quad (3)$$

where A is the amplitude and τ is the decay constant. The pre-spike was sent to the Ti electrode and the post-spike was sent to the Ta electrode; the time difference between the spikes is denoted by Δt . Figure 4b,c show the measurement and simulation of the STDP synapse weight change Δw , which is defined as the percentage change in the cell conductance after the STDP event. If the pre-spike precedes the post-spike ($\Delta t > 0$), the polarity of the net spike is mostly positive, resulting in the potentiating action. If the post-spike precedes the pre-spike ($\Delta t < 0$), the polarity of the net spike is mostly negative, resulting in the depressing action. Furthermore, as Δt decreases, the amplitude of the net spike increases, leading to larger Δw .

Paired-pulse facilitation (PPF) in biological synapses involves temporal summation on inputs, *i.e.* reducing the time interval between two sequential potentiating pulses enhances synaptic weight [32]. This function provides additional flexibility in processing information in the frequency domain. Figure 5 shows the pulse waveform and measurement results for PPF in the Ta/TaO_x/TiO₂/Ti device. The PPF ratio is defined by:

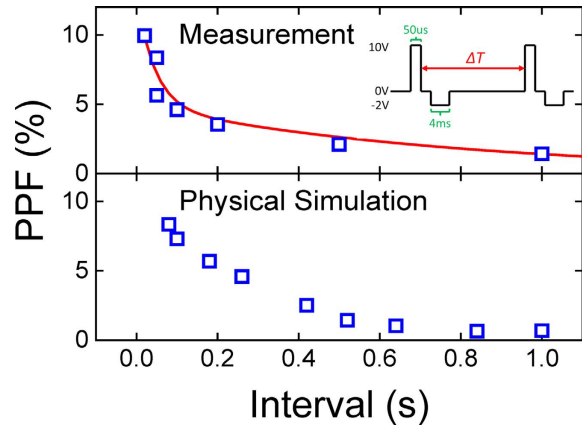


Figure 5. Paired-pulse facilitation (PPF). The inset shows the waveform used for the PPF measurement and simulation. Two identical potentiating pulses, each followed by a negative read pulse, were separated by different time intervals. The PPF ratio is defined as the incremental percentage change in the conductance readouts after the first and second pulses. Both measured and simulated PPF ratios are shown as a function of the time interval between the potentiating pulses. The red line shows the empirical fitting result of using Eq. (4). The two fitting time constants, τ_1 (45 ms) and τ_2 (800 ms) correspond to the fast and slow decaying terms, respectively, and agree with time scales of biological synapses [32].

$$PPF = (G_2 - G_1)/G_1 \times 100\% = C_1 \exp(-t/\tau_1) + C_2 \exp(-t/\tau_2) \quad (4)$$

where G_1 and G_2 are the conductance readouts after the first and second pulses, respectively. The two fitting time constants, τ_1 (45 ms) and τ_2 (800 ms) correspond to the fast and slow decaying terms, respectively. These time scales agree with those of biological synapses [32]. The PPF effect can also be modeled using the HBM model in which O^{2-} diffuses from the Ta/TaO_x interface toward the TaO_x bulk during the time interval between pulses. The simulation results in Fig. 5 also agree with experimental data. The longer the time interval is, the weaker the memory effect of the previous pulse on the consecutive pulse.

Discussion

The I - V characteristics of general memristive devices are described using the following two coupled equations [3]:

$$I = G(g) \cdot V \quad (5)$$

$$\frac{dg}{dt} = f(g, V) \quad (6)$$

where g is an internal state variable. The conductance of memristive devices is determined according to its internal state variable, and the change rate of the internal state variable is determined according to its present state and the applied voltage. On the basis of oxygen ion migration and the HBM model for the Ta/TaO_x/TiO₂/Ti device, a physics-based compact model that complies with the general definition of memristive devices was developed to enable large-scale simulation of neuromorphic systems. The compact model is expressed as:

$$I = I_0 \cdot \exp(-g) \cdot \sinh(V_R) \quad (7)$$

$$\frac{dg}{dt} = \exp\left(-\frac{E_A}{kT}\right) \cdot \sinh[C(g) - \gamma(g) V_W] \quad (8)$$

where V_R and V_W are the read voltage and the potentiating/depressing voltage, respectively. Equation (7) describes the tunnel current through TaO_x during the read operation using a constant I_0 and an effective tunnel gap g . Equation (8) describes the change in g resulting from O^{2-} migration through drift and diffusion processes during potentiation and depression. The velocity of O^{2-} migration is influenced by the local O^{2-} density and the electric field in the present state, which can be obtained only by numerically solving Eqs. (1) and (2) simultaneously. The analytical model represented by Eq. (8) uses two linear fitting functions of g , field-independent function $C(g)$ and field-acceleration function $\gamma(g)$, rather than two constants, to account for the state-dependent velocity of O^{2-} migration. Different $C(g)$ and $\gamma(g)$

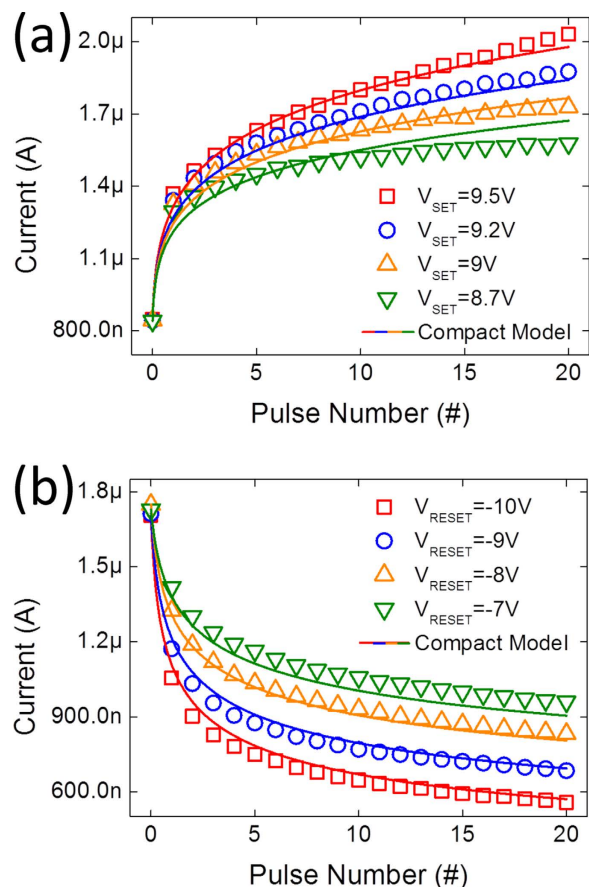


Figure 6. Physics-based compact model fitting. (a) Potentiating and (b) depressing curves of the Ta/TaO_x/TiO₂/Ti device for four pulse amplitudes. The measured data (symbols) and the compact model fitting (lines) are in excellent agreement.

were used for potentiation and depression because the charge distributions and field-acceleration process are different for forward and backward O²⁻ migration. Figure 6a,b show that the compact model fits the potentiating and depressing curves with high accuracy. The fitting accuracy can be increased using higher-order fitting polynomials for $C(g)$ and $\gamma(g)$. Furthermore, this compact model can be applied to simulate STDP characteristics, as shown in Fig. 4b. Because STDP is triggered using a waveform with a time-varying amplitude (See Fig. 4a), the favorable agreement between the measurement and simulation results demonstrates that this compact model is applicable over a wide range of voltages and times.

In summary, the synaptic features of the Ta/TaO_x/TiO₂/Ti device were investigated experimentally and theoretically, for demonstrating the feasibility of the device as a building block in future hardware-based neuromorphic computing systems. The device can be used for implementing concurrent inhibitory and excitatory synapses, and it provides superior performance compared with the typical filamentary synaptic devices in reducing synaptic conductance and state fluctuation. The potentiating and depressing evolution of synaptic states for DC and AC inputs, STDP, and PPF can be satisfactorily explained using the HBM model involving O²⁻ migration. Furthermore, because of the improved physical understanding of the operating mechanism, a compact model based on the general definition of memristive devices accurately describes the measurement results obtained over a wide range of voltages and times.

Methods

The Ta/TaO_x/TiO₂/Ti cell was fabricated using a shadow-mask process and had a device area of 10⁴ μm². The bottom and top electrodes were formed by depositing 100-nm-thick Ti and 100-nm-thick Ta layers through DC magnetron sputtering, respectively. To prepare the bilayer TaO_x/TiO₂ at the bottom electrode, 60-nm-thick TiO₂ and 20-nm-thick TaO_x layers were sequentially deposited through reactive DC magnetron sputtering of metal targets at room temperature in an Ar-O₂ atmosphere. DC electrical characteristics were measured using an Agilent B1500A semiconductor analyzer in a voltage-sweep mode. Pulse measurements were performed using an Agilent B1530A waveform generator/fast measurement unit.

References

1. Mead, C. Neuromorphic electronic systems. *Proc. IEEE* **78**, 1629–1636 (1990).
2. Kuzum, D., Yu, S. & Wong, H.-S. P. Synaptic electronics: materials, devices and applications. *Nanotechnology* **24**, 382001 (2013).
3. Chua, L. & Kang, S. Memristive devices and systems. *Proc. IEEE* **64**, 209–223 (1976).
4. Strukov, D. B., Snider, G. S., Stewart, D. R. & Williams, R. S. The missing memristor found. *Nature* **453**, 80–83 (2008).
5. Choi, H. *et al.* An electrically modifiable synapse array of resistive switching memory. *Nanotechnology* **20**, 345201 (2009).
6. Yu, S., Wu, Y., Jeyasingh, R., Kuzum, D. & Wong, H. P. An electronic synapse device based on metal oxide resistive switching memory for neuromorphic computation. *IEEE Trans. Electron Devices* **58**, 2729–2737 (2011).
7. Suri, M. *et al.* CBRAM devices as binary synapses for low-power stochastic neuromorphic systems: auditory (cochlea) and visual (retina) cognitive processing applications. *IEDM Tech. Dig.* 235–238 (2012).
8. Yu, S. *et al.* Neuromorphic visual system using RRAM synaptic devices with sub-pJ energy and tolerance to variability: Experimental characterization and large-scale modeling. *IEDM Tech. Dig.* 239–242 (2012).
9. Gao, B. *et al.* Ultra-low-energy three-dimensional oxide-based electronic synapses for implementation of robust high-accuracy neuromorphic computation system. *ACS Nano* **8**, 6998–7004 (2014).
10. Chang, T. *et al.* Synaptic behaviors and modeling of a metal oxide memristive device. *Appl. Phys. A* **102**, 857–863 (2011).
11. Jo, S. H., Chang, T., Ebong, I., Bhadviya, B. B., Mazumder, P. & Lu, W. Nanoscale memristor device as synapse in neuromorphic systems. *Nano Lett.* **10**, 1297–301 (2011).
12. Park, S. *et al.* RRAM-based synapse for neuromorphic system with pattern recognition function. *IEDM Tech. Dig.* 231–234 (2012).
13. Park, S. *et al.* Neuromorphic speech systems using advanced ReRAM-based synapse. *IEDM Tech. Dig.* 625–628 (2013).
14. Seo, K. *et al.* Analog memory and spike-timing-dependent plasticity characteristics of a nanoscale titanium oxide bilayer resistive switching device. *Nanotechnology* **22**, 254023 (2011).
15. Govoreanu, B. *et al.* 10×10 nm² Hf/HfO_x crossbar resistive RAM with excellent performance, reliability and low-energy operation. *IEDM Tech. Dig.* 729–732 (2011).
16. Kuzum, D., Jeyasingh, R. G. D., Lee, B. & Wong, H.-S. P. Nanoelectronic programmable synapses based on phase change materials for brain-inspired computing. *Nano Lett.* **12**, 2179–2186 (2011).
17. Suri, M. *et al.* Phase change memory as synapse for ultra-dense neuromorphic systems: application to complex visual pattern extraction. *IEDM Tech. Dig.* 79–82 (2011).
18. Ishiura, H. Proposal of adaptive-learning neuron circuits with ferroelectric analog-memory weights. *Japan. J. Appl. Phys.* **32**, 442–446 (1993).
19. Diorio, C., Hasler, P., Minch, B. A. & Mead, C. A single-transistor silicon synapse. *IEEE Trans. Electron Devices* **58**, 1972–1980 (1996).
20. Waser, R., Dittmann, R., Staikov, G. & Szot, K. Redox-based resistive switching memories -Nanoionic mechanisms, prospects, and challenges. *Adv. Mater.* **21**, 2632–2663 (2009).
21. Goux, L. *et al.* Understanding of the intrinsic characteristics and memory trade-offs of sub-μA filamentary RRAM operation. *Tech. Dig. VLSI Symp. Technol.* 162–163 (2013).
22. Hsu, C.-W. *et al.* Self-rectifying bipolar TaO_x/TiO₂ RRAM with superior endurance over 10¹² cycles for 3D high-density storage-class memory. *Tech. Dig. VLSI Symp. Technol.* 166–167 (2013).
23. Hsu, C.-W. *et al.* Homogeneous barrier modulation of TaO_x/TiO₂ bilayer for ultra-high endurance three-dimensional storage-class memory. *Nanotechnology* **25**, 165202 (2014).
24. Mott, N. F. & Gurney, R. W. *Electronic processes in ionic crystals* (Oxford, 1948).
25. Yu, S. & Wong, H.-S. P. A phenomenological model for the reset mechanism of metal oxide RRAM. *IEEE Electron Dev. Lett.* **31**, 1455–1457 (2010).
26. Kim, S. *et al.* Physical electro-thermal model of resistive switching in bi-layered resistance-change memory. *Sci. Rep.* **3**, 1680 (2013).
27. Kofstad, P. *Nonstoichiometry, diffusion, and electrical conductivity in binary metal oxides* (Wiley-Interscience, 1972).
28. Soerensen, O. T. *Nonstoichiometric oxides* (Academic Press, 2012).
29. Menzel, S., Waters, M., Marchewka, A., Böttger, U., Dittmann, R. & Waser, R. Origin of the ultra-nonlinear switching kinetics in oxide-based resistive switches. *Adv. Funct. Mater.* **21**, 4487–4492 (2011).
30. Zamarreño-Ramos, C. *et al.* On spike-timing-dependent-plasticity, memristive devices, and building a self-learning visual cortex. *Front. Neurosci.* **5**, 26 (2011).
31. Hebb, D. O. *The organization of behavior: A neuropsychological study* (New York, (Wiley, 1949).
32. Zucker, R. S. & Regehr, W. G. Short-term synaptic plasticity. *Annu. Rev. Physiol.* **64**, 355–405 (2002).

Acknowledgements

This work was supported by Ministry of Science and Technology of Taiwan, Republic of China, under grant NSC 102-2221-E-009-188-MY3. T.-H. Hou acknowledges support by NCTU-UCB I-RiCE program, under grant NSC-102-2911-I-009-302. The authors are grateful to the Nano Facility Center at National Chiao Tung University and National Nano Device Laboratories, where the experiments in this paper were performed.

Author Contributions

Y.F.W., T.P.L., and T.H.H. performed the 1D numerical simulation. Y.C.L. and I.T.W. performed electrical measurements and constructed the compact model. I.T.W. fabricated the samples. Y.F.W. and T.H.H. co-wrote the paper. All authors discussed the results and commented on the manuscript.

Additional Information

Supplementary information accompanies this paper at <http://www.nature.com/srep>

Competing financial interests: The authors declare no competing financial interests.

How to cite this article: Wang, Y.-F. *et al.* Characterization and Modeling of Nonfilamentary Ta/TaO_x/TiO₂/Ti Analog Synaptic Device. *Sci. Rep.* **5**, 10150; doi: 10.1038/srep10150 (2015).



This work is licensed under a Creative Commons Attribution 4.0 International License. The images or other third party material in this article are included in the article's Creative Commons license, unless indicated otherwise in the credit line; if the material is not included under the Creative Commons license, users will need to obtain permission from the license holder to reproduce the material. To view a copy of this license, visit <http://creativecommons.org/licenses/by/4.0/>